Supplementary Material: The structure-dynamics feedback mechanism governs the glassy dynamics in epithelial monolayers

Satyam Pandey,[1] Soumitra Kolya,[1] Padmashree Devendran,[1] Souvik Sadhukhan,[1] Tamal Das,[1, *] and Saroj Kumar Nandi[1, †]

[1]*Tata Institute of Fundamental Research, Hyderabad - 500046, India*

In this supplementary material, we provide the simulation details of Vertex models, a brief overview of MCT, the details of the numerical solution, a description of the non-ergodicity transition, wavevector-dependence of the MCT solution, the random first-order transition theory fits of the simulation data, and additional details of the experimental system and their analyses.

SI. VERTEX MODEL OF CONFLUENT TISSUES

The computational models of confluent cell monolayers have an energy function, Eq. (1) in the main text, and they represent cells as polygons [S1–S10]. These models can be both lattice-based or continuum. In this work, we have used a continuum model known as the Vertex model. In this model, the degrees of freedom are the vertices. The vertices in a cell are connected with a straight line to obtain the cell volume and the perimeter.

Figure S1(a) shows a typical configuration from our simulation. Unlike particulate systems, packing fraction in the confluent models remains one at all times and cannot be a control parameter. One particular process, known as the $T1$ transition, is crucial for the dynamics in these systems. A $T1$ transition involves the disappearance of an edge between two neighboring cells followed by the subsequent formation of a perpendicular edge between them (Fig. S1b).
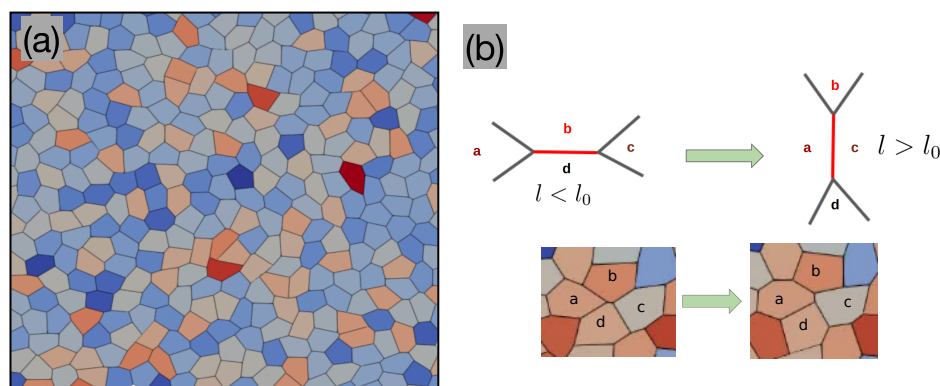

FIG. S1. (a) A snapshot of the Vertex model from our simulation. The polygons represent different cells; colors are for visual presentation. (b) Schematic representation of the $T1$ transition or the neighbor exchange process.

The Vertex model is one of the most widely used systems to study the glassy dynamics in confluent systems. In its usual implementation, three edges meet at each vertex (Fig. S1a). This property remains conserved throughout the dynamics. However, when $p_0 > p_{\min}$, vertices with more number of edges seem to become favorable [S8, S11, S12]. The consequence of this change in property is not yet entirely clear. Therefore, we restricted $p_0 < p_{\min}$ in our simulations.

SII. SIMULATION DETAILS

We have used Brownian dynamics [S13] in our simulations:

$$\gamma\dot{\mathbf{r}}_i = \mathbf{F}_i + \sqrt{2D_T}\zeta, \tag{S1}$$

where D_T is the translational diffusivity at temperature T, γ is the substrate friction, and ζ is a random noise with zero mean and unit variance. The force, $\mathbf{F}_i$, is obtained via the energy function, $\mathcal{H}$, given in the main text [S13].

———————

* tdas@tifrh.res.in
† saroj@tifrh.res.in

We have used a square box of dimension $L = 30$ for our simulations. We first generate a randomized point pattern comprising N non-overlapping points via the random sequential addition algorithm. We use these points as the initial set of seed points for Voronoi tessellation incorporating periodic boundary conditions. We then equilibrate the configuration for the specific values of parameters and use it as the initial configuration for subsequent simulations. During the simulation, we monitored the edge lengths. If an edge becomes smaller than a specified length, l_0, we implemented a $T1$ transition. We ensured that the new edge length after the $T1$ transition was greater than l_0.

Calculating the cell center: As described in the main text, we represent the cells by their centers (of mass). We compute the cell center from the vertex positions. Assuming the vertices come in either clockwise or counterclockwise order, we can calculate the position of the center as

$$\mathbf{r}_{i,x}^{\text{cm}} = \frac{1}{6A} \sum_{i=0}^{n-1} (x_i + x_{i+1})(x_i y_{i+1} - x_{i+1} y_i)$$
$$\mathbf{r}_{i,y}^{\text{cm}} = \frac{1}{6A} \sum_{i=0}^{n-1} (y_i + y_{i+1})(x_i y_{i+1} - x_{i+1} y_i),$$

(S2)

where n is the total number of vertices of a given cell, and the area A is obtained as

$$A = \frac{1}{2} \sum_{i=0}^{n-1} (x_i y_{i+1} - x_{i+1} y_i).$$

(S3)

As the cell perimeter is a closed loop object, we must have $x_0 = x_n$ and $y_0 = y_n$.

SIII.   MODE COUPLING THEORY (MCT)

SIIIA.   Basic form of the theory

The mode Coupling theory (MCT) was first derived for the glassy dynamics of particulate systems [S14–S16]. It is a first-principle analytical theory for an immensely complex system. Here, we briefly highlight the main features of the theory. Consider the Hamiltonian H for a particulate system,

$$H = \sum_i \frac{p_i^2}{2m} + \frac{1}{2} \sum_{i,j \neq i} \phi(r_{ij}),$$

(S4)

where p_i is the momentum of the ith particle (not to confuse with the perimeter of cell), m, the mass, r_{ij}, the inter-particle distance between the ith and the jth particles, ϕ is the interaction potential. We can then write down the equation of motion for any variable $A(t)$ as

$$\frac{dA(t)}{dt} = \{A(t), H\} = i\mathcal{L}A(t)$$

(S5)

where $\mathcal{L}$ is Liouville operator [S16]. The number density in real space is

$$\rho(r,t) = \sum_j^N \delta(r - r_j(t))$$

(S6)

and in Fourier space, $\rho(k,t)$ is

$$\rho(k,t) = \sum_j^N \exp(ikr_j(t))$$

(S7)

where N is the total number of particles and $r_j(t)$ is the position of particle j at time t. The intermediate scattering function $F(k,t)$ is

$$F(k,t) = \frac{1}{N} \langle \rho(-k,0)\rho(k,t) \rangle$$

(S8)

where the bracket denotes the ensemble average. The static structure factor $S(k)$ is

$$S(k) = \frac{1}{N} \langle \rho(-k,0)\rho(k,0) \rangle. \tag{S9}$$

Using Eq. (S5) with $A(t) = (\rho(k,t), j(k,t))$, we can use the Mori-Zwanzig projection formalism to write down the equation of motion for $F(k,t)$ as

$$\frac{\partial}{\partial t}F(k,t) + \frac{D_0 k^2}{S(k)}F(k,t) + \int_0^t dt' M(k, t-t')\frac{\partial}{\partial t}F(k,t') = 0, \tag{S10}$$

where $S(k)$ is static structure factor (center-of-mass) of cells in confluent epithelial monolayer, D_0 is equal to $k_B T/m$ and $M(k,t)$ is the Memory kernel can be written as

$$M(k,t) = \frac{\rho D_0}{2} \int \frac{d\boldsymbol{q}}{(2\pi)^2} V_k^2(\boldsymbol{q}, \mathbf{k}-\mathbf{q})F(|\boldsymbol{k}-\boldsymbol{q}|, t)F(\boldsymbol{q}, t), \tag{S11}$$

where ρ is number density and V_k is the vertex function can be written as

$$V(\boldsymbol{q}, \mathbf{k}-\mathbf{q}) = \hat{k}.\boldsymbol{q}c(q) + \hat{k}.(\mathbf{k}-\mathbf{q})c(|\mathbf{k}-\mathbf{q}|) \tag{S12}$$

where $c(q)$ is the direct correlation function. Equation (S10) is a non-linear integro-differential equation that we can self-consistently solve with a static structure factor as an input. Note the generic features of the mode-coupling theory:

- Equation (S10) is quite generic: it is applicable for any dimension and any system in the absence of external fields.

- The potential ϕ can have an arbitrary form. Therefore, the theory is also applicable to the confluent system. ϕ in Eq. (S4) corresponds to $\mathcal{H}$ in the main text.

- The information of the system enters via ϕ alone; this is encoded through $S(k)$ in Eq. (S10). Solution of the MCT equation requires $S(k)$ as the input, it acts as the initial condition, $F(k, t=0) = S(k)$.

SIIIB.   MCT in two-dimension

We are interested in spatial dimension two ($2d$) for the confluent epithelial monolayers. Equation S10 can be written in $2d$ as,

$$\tau_k \frac{\partial}{\partial t}f(k,t) + f(k,t) + \int_0^t dt' m(k, t-t')\frac{\partial}{\partial t}f(k,t') = 0, \tag{S13}$$

where $\tau_k = S(k)/D_0 k^2$, $f(k,t) = F(k,t)/S(k)$, and

$$m(k,t) = \frac{1}{2\rho k^2} \int \frac{d\boldsymbol{q}}{(2\pi)^2} V_k^2(\mathbf{q}, \mathbf{k}-\mathbf{q})S(k)S(|\mathbf{q}-\mathbf{k}|)S(q)f(|\mathbf{q}-\mathbf{k}|, t)f(\mathbf{q}, t). \tag{S14}$$

For the convenience of discretization, we rewrite the kernel in symmetrized form as

$$m(k,t) = \frac{1}{2\rho k^2} \int \frac{d\boldsymbol{q}}{(2\pi)^2} V^2(k/2+q, k/2-q)S(k)S(|\mathbf{k}/2+\mathbf{q}|)S(|\mathbf{k}/2-\mathbf{q}|)f(|\mathbf{k}/2-\mathbf{q}|, t)f(|\mathbf{k}/2-\mathbf{q}|, t). \tag{S15}$$

We now use the change of variables as

$$x = |\mathbf{k}/2+\mathbf{q}| = \sqrt{(q_x+k/2)^2 + q_y^2} = \sqrt{q^2 + kq\cos\theta + \frac{k^2}{4}}$$

$$y = |\mathbf{k}/2-\mathbf{q}| = \sqrt{(q_x-k/2)^2 + q_y^2} = \sqrt{q^2 - kq\cos\theta + \frac{k^2}{4}}, \tag{S16}$$

where θ is the angle between k and q. As a result, the memory kernel becomes

$$m(k,t) = \frac{\rho}{8\pi^2 k^4} \int_0^{k_m} dx \int_{|k-x|}^{|x+k|} dy\, xy S(k)S(x)S(y) \frac{[(k^2+x^2-y^2)c(x) + (k^2-x^2+y^2)c(y)]^2}{(((4x^2 k^2) - ((k^2+x^2-y^2)^2)^{\frac{1}{2}})} f(x,t)f(y,t) \tag{S17}$$

where k_m is the numerical cut off wave vector and c and S are related by the Ornstein-Zernike [S17] equation,

$$c(k) = \frac{1}{\rho}\left(1 - \frac{1}{S(k)}\right).$$

(S18)

Details of the parameters for the numerical solution: For the numerical solution, we follow the algorithm developed by Fuchs et al. [S18]. $F(k,t)$ decays very fast at short times and quite slow at long times. Therefore, to numerically resolve both regimes, we must use an adaptive step size to discretize t. Thus, we start with a small time step $h = 10^{-8}$ and double the step size every $N_t = 128$ time step. We have discretized k via an equally spaced grid of $N_k = 200$ points with a grid spacing $\Delta k = 0.2$. So our wave vector grid become $(i_k \times \Delta k)$ where i_k runs from 1 to N_k. We write the memory kernel, Eq. (S17), using the discrete Riemann sums,

$$\int_0^{k_m} dx \int_{|k-x|}^{x+k} dy.... \rightarrow \sum_{i_x=1}^{N_k}(\Delta k)\sum_{y=|k-x|}^{|k+x|}(\Delta k).$$

(S19)

There is a divergence in the two extreme limits; we computed the sum by avoiding these points with respect to our k-discretization.

SIIIC. The non-ergodicity transition of MCT

As we have discussed in the main text, MCT works surprisingly well in a specific regime of parameter space. At high T, $F(k,t)$ quickly decays to zero. As we decrease T, the time evolution of $F(k,t)$ becomes slower. It first decays to a plateau and then towards zero at long times. As we further decrease T, $F(k,t)$ never becomes zero and remains stuck at a finite value forever; this is the non-ergodicity transition of MCT. The reason behind this transition remains unclear. It is generally believed that MCT is a mean-field theory; the sharp MCT transition becomes a crossover for finite-dimensional systems. However, the glassy properties are still governed by this genuine phase transition.

This transition should persist in confluent systems too. As Fig. S2 shows, the decay of $F(k_{\max},t)$ becomes slower as T becomes lower and eventually, at a low enough T which is T_{MCT}, $F(k_{\max},t)$ does not decay to zero.
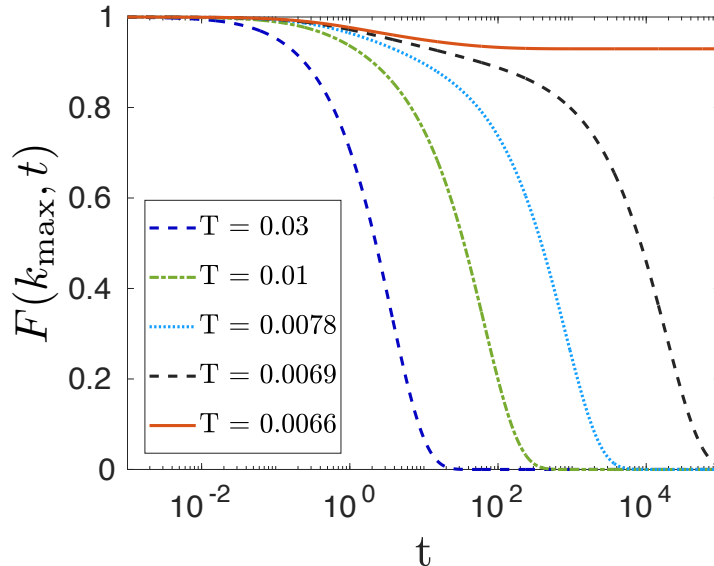

FIG. S2. The non-ergodicity transition of MCT. As T decreases, the decay of $F(k_{\max},t)$ becomes slower. When $T = T_{\mathrm{MCT}}$, the correlation function remains fixed at a finite value.

SIIID. k-dependence of $F(k,t)$

We have discussed in the main text that the precise nature of the decay of $F(k,t)$ depends on the specific value of k. We have chosen six different values of k and show the decay of $F(k,t)$ for these values of k.
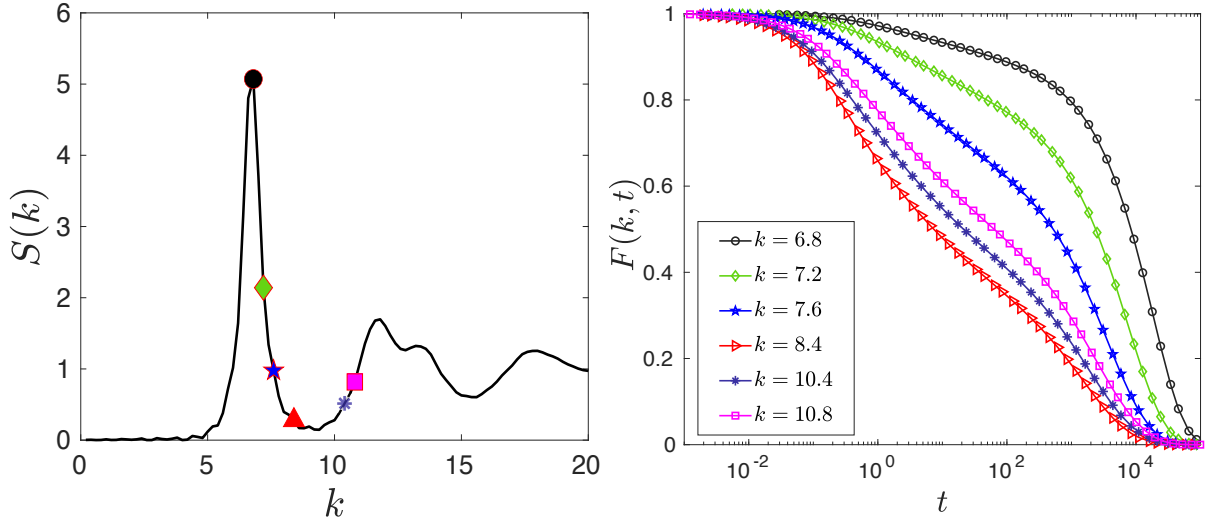

FIG. S3. Wavevector-dependence of $F(k,t)$. (a) We use the $S(k)$ for $T = 0.0069$ and $p_0 = 3.52$ as input to MCT to obtain $F(k,t)$. (b) The decay of $F(k,t)$ corresponding to the values of k is shown by the symbols in (a). The precise nature of $F(k,t)$ depends on the specific values of k.

SIIIE. k and a-dependence of the value of τ in MCT and simulation
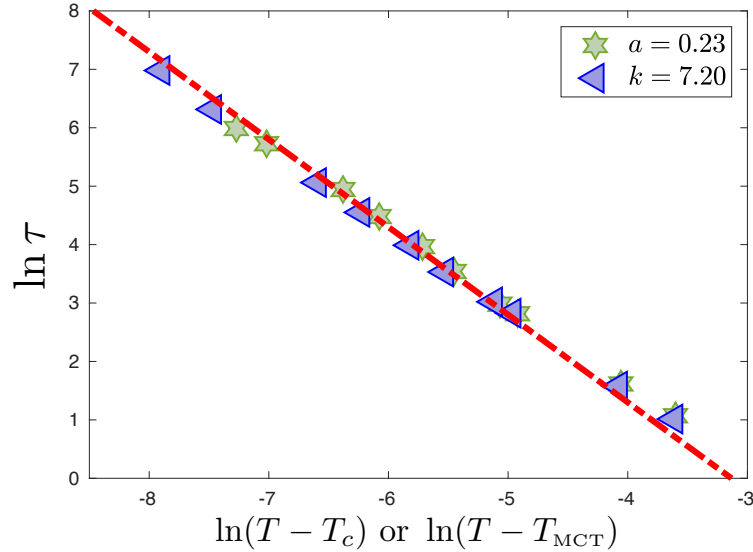

FIG. S4. We have tuned k and a in such a way that the τ for the same parameters becomes the same. We have used $p_0 = 3.70$, $k = 7.2$, and $a = 0.23$.

The precise values of τ in MCT and simulation depend on k and a, respectively. However, their trends are independent of these parameters. Moreover, we can tune them k and a to have the same numerical values of τ. The specific choices of k and a are motivated by practical considerations for better analysis. We demonstrate in Fig. S4 that for suitable choices of k and a,

we can have similar values of τ within MCT and simulation. However, these parameters are not computationally convenient; therefore, we chose a different set of values, as stated in the main text.

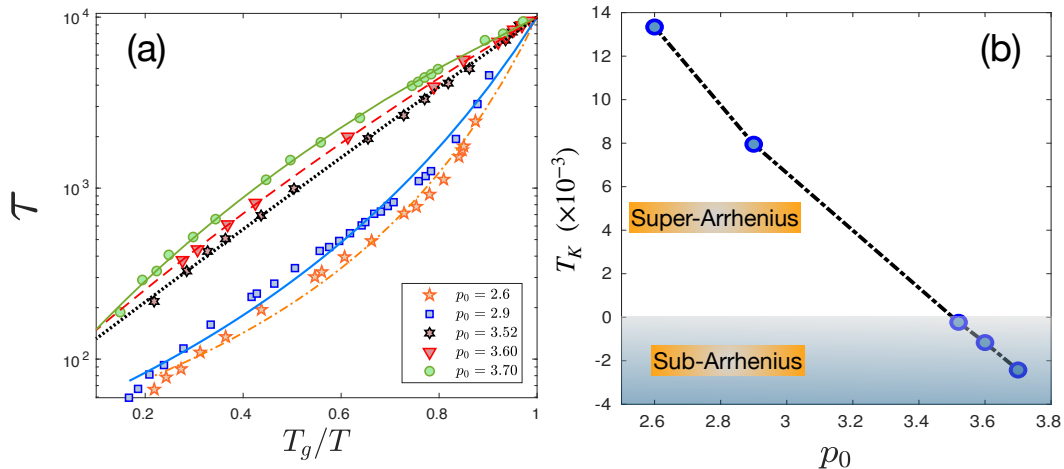### SIIIF. RFOT theory fits for the sub- and super-Arrhenius relaxations

FIG. S5. Application of the RFOT theory to the simulation data. (a) Fit of the RFOT theory form, Eq. (S20), with the simulation data gives a reasonable description of the data. (b) T_K in the sub-Arrhenius regime becomes negative, showing that the theory is not applicable in this regime.

Compared to the MCT, RFOT theory describes the relaxation dynamics as an activation process over a barrier. The relaxation time is obtained [S19–S21] as

$$\tau = \tau_0 \exp\left[\frac{E}{T - T_K}\right], \tag{S20}$$

where T_K is the Kauzmann temperature, E is a constant, and τ_0 is the high-T value of τ. RFOT theory crucially relies on the existence of a finite-temperature thermodynamic transition at T_K. As shown in Ref. [S22], we can phenomenologically extend the theory for confined systems.

Instead, we can consider an equilibrium scenario where confluency modifies the various constants. Then, we can fit Eq. (S20) with the simulation data treating the constants τ_0, E, and T_K as fitting parameters. We show the fit in Fig. S5(a) and the values of T_K in Fig. S5(b). Consistent with Ref. [S22], we find T_K is negative in the sub-Arrhenius regime and positive in the super-Arrhenius regime, although the fits with the simulation data remain reasonable. The negative T_K implies that the RFOT theory is not applicable in the sub-Arrhenius regime.

SIV. EXPERIMENTAL DETAILS AND ADDITIONAL RESULTS

We conducted the cell culture experiment using Madin-Darby Canine Kidney (MDCK) epithelial cells in culture inserts with three wells (Ibidi chamber). We cultured the MDCK cells in Dulbecco's Modified Eagle Medium (DMEM) supplemented with 5% fetal bovine serum (FBS) and 1% antibiotic (penicillin and streptomycin). The incubation conditions are 37^0C and 5% CO_2. We seeded the cells at different concentrations to achieve variable cell number densities. After the monolayer becomes confluent, we start the imaging process. Before imaging, we replaced the existing cell culture media with fresh media.

SIVA. Imaging

We started imaging using a Leica DMi8 inverted microscope with a 20x objective lens. Images were captured in phase contrast mode at intervals of 2.5 minutes throughout a 4-hour duration. We show a fast-forwarded 4-hour-long imaging video in 6 seconds in Supplementary Movie (SI movie) I. Throughout the microscopy session, we maintained a stable environmental condition of 37^0C with 5% CO_2, achieved by an incubation system mounted over the microscope.
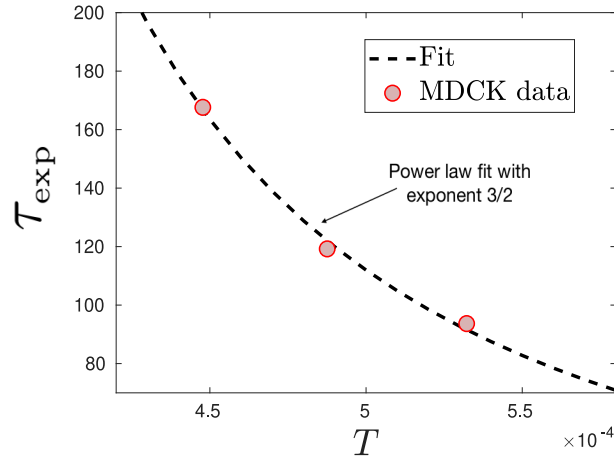
FIG. S6. We fit the experimental data of relaxation time as a function of T (obtained via the Cell Shape Theory, see main text for details) with a power law with exponent $3/2$ that MCT predicts. The data seems to be consistent with this prediction of the theory.

SIVB. Image Analysis and Cell Tracking

After we have the microscopy images, we analyse them to obtain quantitative data. We conducted image analysis using the freely available Cellpose software [S23] and an in-house custom-made code that we developed in MATLAB and Python. We primarily performed cellular segmentation using the Cellpose software and trained our custom segmentation model based on Cellpose 2.0 [S24]. The performance of our trained model is robust; we show in Supplementary Movie II the track of the segmented images corresponding to the movie in SI Movie I. We tracked the cells using the TrackMate [S25] plugin in Fiji [S26].
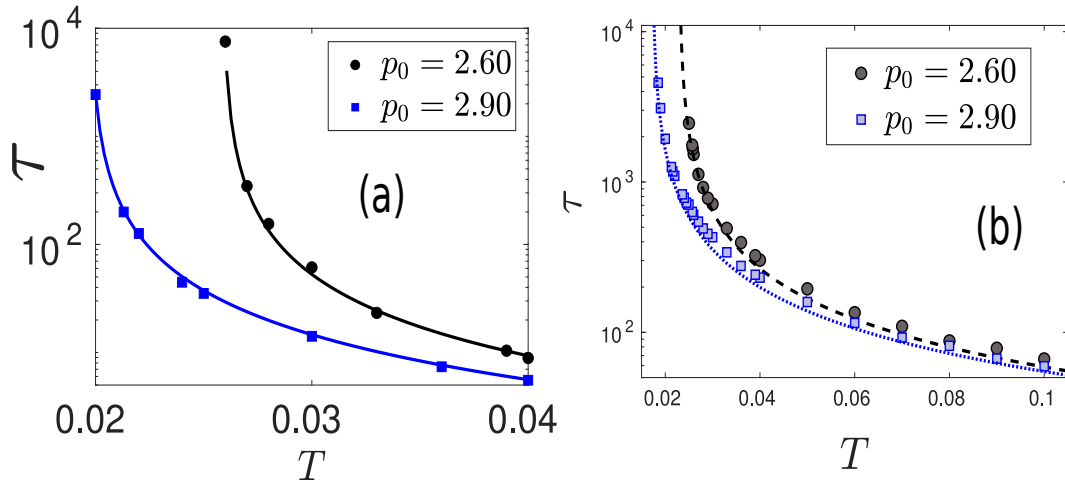

FIG. S7. We fit the simulation data of the relaxation time at low p_0, where the system shows super-Arrhenius behavior, namely at $p_0 = 2.60$ and $p_0 = 2.90$, as a function of T, with a power law with an exponent of 1.

SIVC. Power-law behavior of the relaxation time in experiment

Since we could only get three data points for varying density, it is hard to reliably estimate the power law exponent from fit. However, we confirmed that the exponent $3/2$, as we obtained from MCT, is consistent with the experimental data (Fig. S6).

SIVD. Power-law behavior of the relaxation time in Simuation at low p_0

At lower p_0 values, where the system exhibits super-Arrhenius behavior, although the relaxation dynamics still follow a power-law (Fig.S7), the exponent of the power law depends on p_0 (see main text for details).

SIVE. Cell-shape Distribution (CSD) Function at Constant λ_P/T

At a constant $p_0 = 3.6$, the cell-shape distribution (CSD) function falls onto a single curve for varying λ_p and T such that the ratio of $\lambda_P/T = 2.78$ remains constant (Fig.S8). We obtain $\alpha = 6.09$ by fitting the data with CSD function. This shows that a change in λ_P can be represented via a corresponding change in T.
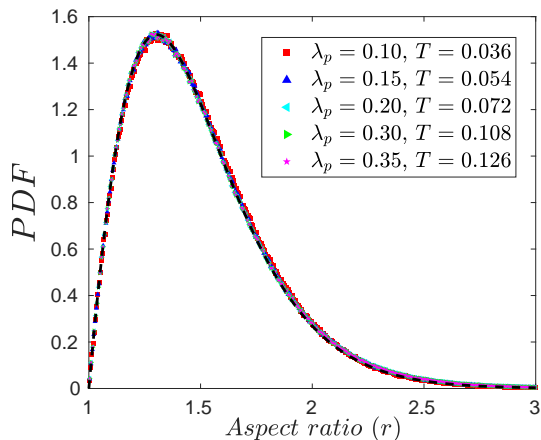

FIG. S8. Cell-shape distribution (CSD) function at $p_0 = 3.60$ and constant $\lambda_P/T = 2.78$ for various λ_P and T. We obtain the values of $\alpha = 6.09$ by fitting the data with the CSD function.

SIVF. Fit of τ_{MCT} vs τ_{exp} data with a homogeneous form
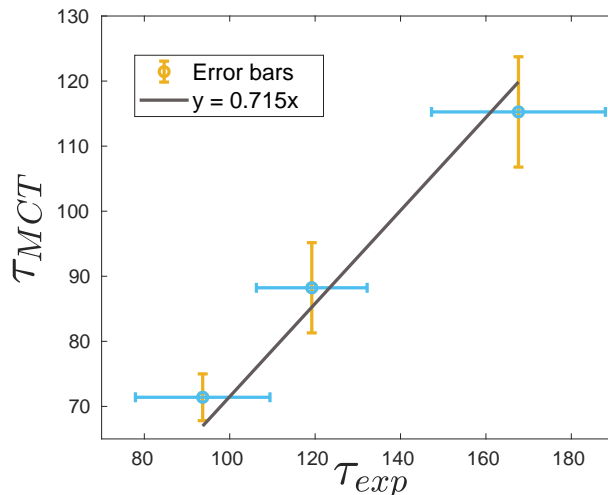

FIG. S9. A homogeneous form for $\tau_{\text{MCT}} = C\tau_{\text{exp}}$ with $C = 0.72$ also fits well with the data. The line is within the error bars of the data.

[S1] H. Honda and G. Eguchi, J. Theor. Biol. **84**, 575 (1980).

[S2] M. Marder, Phys. Rev. A **36**, 438(R) (1987).

[S3] F. Graner and J. A. Glazier, Phys. Rev. Lett. **69**, 2013 (1992).

[S4] J. A. Glazier and F. Graner, Phys. Rev. E **47**, 2128 (1993).

[S5] T. Hirashima, E. G. Rens, and R. M. H. Merks, Develop. Growth Differ. **59**, 329 (2017).

[S6] P. Hogeweg, J. Theor. Biol. **203**, 317 (2000).

[S7] R. Farhadifar, J.-C. Röper, B. Aigouy, S. Eaton, and F. Jülicher, Curr. Biol. **17**, 2095 (2007).

[S8] D. B. Staple, R. Farhadifar, J.-C. Röper, B. Aigouy, S. Eaton, and F. Jülicher, The European Physical Journal E **33**, 117 (2010).

[S9] A. Fletcher, M. Osterfield, R. Baker, and S. Shvartsman, Biophys. J. **106**, 2291 (2014).

[S10] D. L. Barton, S. Henkes, C. J. Weijer, and R. Sknepnek, PLOS Computational Biology **13**, 1 (2017).

[S11] K. E. Kasza, D. L. Farrell, and J. A. Zallen, Proc. Natl. Acad. Sci. (USA) **111**, 11732 (2014).

[S12] L. Yan and D. Bi, Phys. Rev. X **9**, 011029 (2019).

[S13] S. Tong, N. K. Singh, R. Sknepnek, and A. Košmrlj, PLOS Computational Biology **18**, 1 (2022).

[S14] W. Götze, *Complex Dynamics of Glass-Forming Liquids: A Mode-Coupling Theory* (Oxford University Press, 2008).

[S15] S. P. Das, Rev. Mod. Phys. **76**, 785 (2004).

[S16] D. R. Reichman and P. Charbonneau, J. Stat. Mech. , P05013 (2005).

[S17] J.-P. Hansen and I. R. McDonald, *Theory of Simple Liquids*, 4th ed. (Elsevier, 2013).

[S18] T. Franosch, M. Fuchs, W. Götze, M. R. Mayr, and A. P. Singh, Phys. Rev. Lett. **55**, 7153 (1997).

[S19] V. Lubchenko and P. G. Wolynes, Ann. Rev. Phys. Chem. **58**, 235 (2007).

[S20] G. Biroli and J. P. Bouchaud, in *Structural Glasses and Supercooled Liquids: Theory, Experiment, and Applications*, edited by P. G. Wolynes and V. Lubchenko (2012).

[S21] T. R. Kirkpatrick and D. Thirumalai, Rev. Mod. Phys. **87**, 183 (2015).

[S22] S. Sadhukhan and S. K. Nandi, Phys. Rev. E **103**, 062403 (2021).

[S23] C. Stringer, T. Wang, M. Michaelos, and M. Pachitariu, Nature Methods **18**, 100 (2021).

[S24] M. Pachitariu and C. Stringer, Nature Methods **19**, 1634 (2022).

[S25] D. Ershov, M.-S. Phan, J. W. Pylvänäinen, S. U. Rigaud, L. Le Blanc, A. Charles-Orszag, J. R. W. Conway, R. F. Laine, N. H. Roy, D. Bonazzi, G. Duménil, G. Jacquemet, and J.-Y. Tinevez, Nature Methods **19**, 829 (2022).

[S26] J. Schindelin, I. Arganda-Carreras, E. Frise, V. Kaynig, M. Longair, T. Pietzsch, S. Preibisch, C. Rueden, S. Saalfeld, B. Schmid, J.-Y. Tinevez, D. J. White, V. Hartenstein, K. Eliceiri, P. Tomancak, and A. Cardona, Nature Methods **9**, 676 (2012).